



1 **Sensitivity of Marine Cloud Brightening over the Great**
2 **Barrier Reef to Spatial Variability in Aerosol Forcing: A Case**
3 **Study using convection-permitting model**

4

5

6

7

Wenhui Zhao¹, Yi Huang^{1,2}, Steven Siems^{2,3}, Daniel Harrison⁴

8

9 ¹School of Geography, Earth and Atmospheric Science, The University of Melbourne, Melbourne, VIC,
10 Australia

11 ²Australian Research Council (ARC) Centre of Excellence for 21st Century Weather, Melbourne, VIC,
12 Australia

13 ³School of Earth, Atmosphere and Environment, Monash University, Melbourne, VIC, Australia

14 ⁴National Marine Science Centre, Southern Cross University, Coffs Harbour, NSW, Australia

15 Correspondence to: Wenhui Zhao (Wenhui.zhao@unimelb.edu.au), and Yi Huang (yi.huang4@unimelb.edu.au)



16 **Abstract.** The Great Barrier Reef (GBR) is increasingly threatened by mass thermal coral bleaching events under
17 climate change. Marine cloud brightening (MCB) has been proposed as a potential adaptation strategy to reduce
18 thermal stress by enhancing cloud reflectivity through aerosol injection. This study evaluates the sensitivity of
19 cloud–aerosol interactions to aerosol emission intensity and spatial configuration over the GBR using convection-
20 permitting Weather Research and Forecasting (WRF) model simulations.

21 A control simulation representing a non- to weakly-precipitating shallow trade-cumulus regime is compared with
22 three MCB sensitivity experiments: a densely distributed (20 km apart), moderate-intensity emission scenario
23 (EXP20), a sparsely distributed (100 km spacing), high-intensity scenario (EXP100), and an intermediate
24 configuration (EXP40). Results show that enhanced aerosol emissions substantially increase near-surface aerosol
25 concentrations, with dispersion strongly governed by source spacing and prevailing trade winds. The EXP20
26 configuration produces more homogeneous and widespread aerosol enhancements, whereas EXP100 generates
27 localized peaks that are rapidly scavenged, resulting in smaller domain-mean increases despite identical total
28 emissions.

29 Over a 24-hour period, domain-averaged cloud droplet number concentration (CDNC), optical depth, and cloud
30 albedo exhibit strong sensitivity to aerosol loading, while cloud water path (CWP) and cloud fraction show limited
31 responses. These findings indicate a dominant Twomey effect in this cloud regime, with only weak evidence of
32 the Albrecht effect. Nonlinear CWP responses are noted under varying conditions of mid-level humidity, wind
33 shear, and lower-tropospheric stability. Overall, the results highlight the importance of aerosol source
34 configuration and background atmospheric state in shaping MCB effectiveness over the GBR.



35 **1 Introduction**

36 The Great Barrier Reef (GBR) has become increasingly vulnerable to more frequent and severe mass thermal
37 coral bleaching events (CBEs) over the past decade (AIMS, 2024; Hughes et al., 2017). Since 1998, eight major
38 thermal CBEs have been recorded over the GBR, six of which have occurred since 2016 (AIMS, 2026). While
39 oceanic warming is a primary driver of bleaching, local cloud cover plays a pivotal role in modulating the surface
40 heat budget over the reef by regulating radiative fluxes. Across the GBR, variations in local cloudiness have been
41 identified as a key factor in controlling the intensity of incoming solar radiation and sea surface temperatures,
42 largely independent of the effects from large-scale climate drivers (Zhao et al., 2021; Richards et al., 2024). These
43 findings underscore that maintaining or enhancing cloud shading over the reef could help moderate extreme
44 warming of the shallow reef waters.

45 Marine Cloud Brightening (MCB) has been proposed as a localized climate intervention strategy to increase cloud
46 reflectivity and provide shading for vulnerable ecosystems like coral reefs (Latham et al., 2008; 2013; Ahlm et al.,
47 2017; Harrison, 2024). By injecting aerosol particles (such as sea-salt spray) that act as cloud condensation nuclei
48 (CCN) into marine warm clouds, MCB aims to increase cloud droplet number concentrations, yielding clouds
49 with smaller droplet sizes and higher optical thickness for the same liquid water content. The result is a brighter
50 cloud that reflects more sunlight back to space, thereby reducing the net solar radiation reaching the ocean surface
51 (Twomey, 1977). In addition, by suppressing warm-rain formation, added CCN can potentially increase cloud
52 longevity and coverage, known as the cloud lifetime effect (Albrecht, 1989). MCB was initially envisioned as a
53 global climate intervention (Latham, 1990; 2002), but more recent efforts have considered targeted regional
54 applications to protect sensitive areas such as the GBR (Latham et al., 2013; Harrison et al., 2025; Hernandez-
55 Jaramillo et al., 2025). Notably, the first field trials of MCB were conducted on the GBR in 2020–2021 (Tollefson,
56 2021), and a dedicated research program is ongoing to assess its feasibility under the Reef Restoration and
57 Adaptation Program (Condie et al., 2021; Harrison, 2023; Baresi et al., 2025). Early observational evidence
58 provides initial insights: a recent airborne study over the GBR found that summertime cumulus clouds in the
59 region were associated with differences in droplet number and size under varying aerosol conditions, with polluted
60 air masses linked to smaller, more numerous cloud droplets and lower rainfall from warm clouds (Hernandez-
61 Jaramillo et al., 2024; Braga et al., 2025). While these contrasts do not isolate aerosol perturbations from
62 concurrent meteorological variability, they are consistent with the expected microphysical responses to enhanced
63 aerosol conditions and suggest that GBR cloud systems are indeed amenable to brightening through aerosol
64 seeding, in line with the physical basis of MCB. However, despite this growing body of observational evidence
65 and the emergence of real-world field testing, critical questions remain regarding the efficiency, spatial extent,
66 and persistence of MCB induced cloud responses at regional scales (Wood and Ackerman, 2013).

67 One key question is how effective deliberate aerosol injections would be in enhancing cloud reflectivity and
68 reducing surface heating, given the complex, nonlinear response of cloud systems to aerosols (Ackerman et al.,
69 2004; Rosenfeld et al., 2019). For instance, in humid and weakly sheared environments, additional aerosols might
70 increase cloud water by suppressing drizzle (Twomey, 1977; Albrecht, 1989), whereas in dry, strongly subsiding
71 environments, the same aerosol addition could reduce cloud liquid water via enhanced entrainment of dry air
72 (Ackerman et al., 2004). The overall radiative benefit therefore depends not only on the magnitude of aerosol-
73 induced microphysical changes but also on the interplay between meteorological variability, boundary-layer
74 dynamics, and potential feedbacks on cloud lifetime and precipitation efficiency. Another open question is how
75 the spatial distribution of aerosol sources influences MCB efficacy. A given total aerosol emission could be
76 delivered by many small, closely spaced sprayers or a few large, widely spaced sprayers, it is unclear which
77 approach yields a greater cloud brightening effect over a region. Understanding these sensitivities is crucial for
78 designing optimal deployment strategies and planning future MCB experiments with a consideration of energy
79 and cost saving.

80 To address these questions, we employ convection-permitting numerical simulations focused on a region of the
81 GBR. High-resolution models (cloud-resolving to kilometre-scale) are suited to capture some of the detailed cloud
82 microphysical responses to aerosol perturbations (Stevens and Feingold, 2009; Dagan et al., 2016; Zhao et al.,
83 2024; Saffin et al., 2023) while still encompassing the mesoscale context of the reef environment. In this study,
84 we use the Weather Research and Forecasting (WRF) model with a sophisticated aerosol-aware microphysics



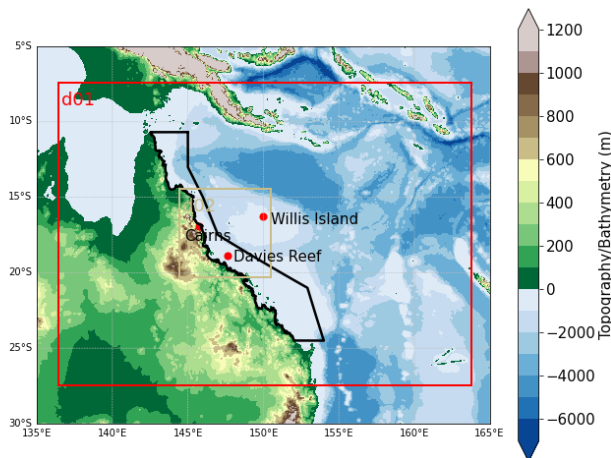
85 scheme to conduct a set of case study simulations. We assess how marine shallow cloud fields over the GBR
86 respond to different spatial configurations of aerosol emissions. By comparing a control case with no seeding to
87 a series of seeding configurations, we examine the sensitivity of cloud droplet population, cloud water content,
88 cloud fraction, and cloud optical properties to aerosol injection patterns. We also explore how meteorological
89 factors modulate the cloud responses. The aim is to provide new insight into the potential effectiveness of MCB
90 over the GBR and to identify the environmental conditions and deployment strategies most conducive to achieving
91 a beneficial increase in cloud reflectivity.



92 **2 Methodology**

93 **2.1 Model configuration**

94 In this study, a convection-permitting numerical model is employed to simulate aerosol-cloud interactions over
 95 the GBR region. Specifically, the simulations are conducted with the Weather Research and Forecasting (WRF,
 96 version 4.2) model, where two nested domains (denoted d01 and d02) are employed with horizontal grid spacings
 97 of 5 km and 1 km, respectively. The outer domain (5 km resolution) covers a large portion of the Northeast
 98 Australian coast and adjacent Coral Sea, while the inner domain (1 km resolution) is centred on the central GBR
 99 around the Cairns region (Figure 1). All simulations employ a vertical grid with 65 unevenly distributed levels,
 100 with finer spacing in the boundary layer (30 levels below 3km) to resolve cloud layers.



101

102 **Figure 1: Nested domain configuration applied in all WRF simulations in this study. Coloring represents the**
 103 **topography-bathymetry of the domain. Black polygon outlines the GBR region.**

104 **Table 1: Configuration settings for numerical simulations conducted in this study**

Parameterisation	Option No. (d01, d02, d03)	Comments
Microphysics	mp_physics = 28	Thompson Aerosol Aware (2014) scheme
PBL	bl_pbl_physics = 1	YSU PBL scheme
Cumulus	cu_physics = 1 (d01 only)	Kain-Fritsch scheme (d01 only)
Land/Sea surface	sf_surface_physics = 2	Noah Land Surface Model
Short wave radiation	ra_sw_physics = 4	RRTMG shortwave
Long wave radiation	ra_lw_physics = 4	RRTMG scheme



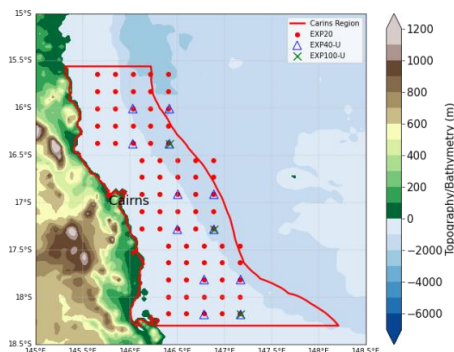
105 All simulations are initialized at 00:00 UTC on 6 Feb 2024 and running for 3 days, with the first 12 hours used as
106 spin-up time. The model uses the fifth-generation atmospheric reanalysis (hourly, $0.25^\circ \times 0.25^\circ$ grid, 37 set
107 pressure levels and surface level) from the European Centre for Medium Range Weather Forecast (ERA5
108 reanalysis, Hersbach et al., 2018; 2020) for initial and lateral boundary conditions. Following initialization, the
109 model is allowed to run freely with no nudging applied, which enables the meteorology to fully develop
110 throughout the simulation. Model prediction output history intervals are 3-hour for d01 and 1-hour for the d02.
111 The analysis in this study focuses on the high-resolution (1 km) inner domain unless otherwise noted.

112 An overview of the parameterization schemes used in the CTRL simulation is shown in Table 1, with the same
113 configuration settings being applied to all sensitivity experiments. Note that this configuration has been tested and
114 demonstrated to exhibit high skill in predicting the marine shallow clouds over the GBR (Zhao et al., 2024). In
115 this configuration, we use the Thompson Aerosol Aware microphysics scheme (Thompson and Eidhammer, 2014),
116 Yonsei University planetary boundary layer scheme (YSU, Hong et al., 2006, first-order nonlocal), "Noah" land
117 surface model (Chen and Dudhia, 2001), and the RRTMG scheme for shortwave and longwave radiation (Mlawer
118 et al., 1997) are applied for each domain. The Kain-Fritsch cumulus parameterisation (Janjić 2000) is only used
119 for the coarse domain (d01) to represent sub-grid convection. The Thompson Aerosol Aware microphysical
120 parameterization uses an auxiliary aerosol climatology as the aerosol background condition placed into WRF
121 model for every grid point, rather than assuming all model horizontal grid points have the same vertical profiles
122 of aerosols. This aerosol climatology is derived from multiyear (2001-2007) global model simulations (Colarco
123 et al., 2010) in which particles and their precursors are emitted by natural and anthropogenic sources. Note that,
124 in this study, the February aerosol climatology value is scaled down by a factor of four for model initialization to
125 represent a more pristine, trade-wind dominated scenario. The unscaled February climatology is strongly
126 influenced by continental aerosol populations and is biased high compared to typical maritime conditions over the
127 GBR. This adjustment is therefore grounded in in-situ observations from a recent field campaign, which reported
128 very low background CCN concentrations ($\sim 180 \text{ cm}^{-3}$ near the surface) over the GBR during prevailing trade flow
129 conditions (Hernandez-Jaramillo et al., 2024; Braga et al. 2025). For example, the unscaled February climatology
130 produces an aerosol number concentration of $\sim 750 \text{ cm}^{-3}$ over the Cairns Region, substantially higher than
131 observations; scaling by one quarter reduces this to $\sim 190 \text{ cm}^{-3}$.

132 2.2 Sensitivity experiments

133 In this study, three sensitivity experiments are undertaken to examine the impact of aerosol source spacing and
134 emission strength on cloud-aerosol interactions over the Cairns region of the GBR. In all three experiments, an
135 identical total aerosol emission flux (7.5×10^{17} particles per second) is introduced into the model, but the number
136 of emission points and the per-source emission rate are varied. In all cases, additional emissions occur only at the
137 surface (the lowest model layer), simulating spray released at the ocean surface, representing continuous operation
138 of MCB sprayers releasing sea-salt aerosol into the marine boundary layer.

139 In each sensitivity experiment, the total aerosol emission flux is distributed equally among the different total
140 number of point sources in the scenario (Figure 2). Specifically, in the dense experiment, namely EXP20, an
141 additional aerosol flux of the 1×10^{16} particles per second is added to climatological surface emission of water-
142 friendly aerosols at each of 75 source points, which are distributed at a fine spatial spacing of 20 km. This setup
143 represents a scenario with more densely distributed aerosol sources, but with relatively lower increased localized
144 aerosol emissions. The second experiment, EXP40, uses 12 point sources spaced 40 km apart, 3 sets of 4 stations
145 aligned along the predominant axis of wind (Figure 2, blue triangles). Each source in this case emits 6.25×10^{16}
146 particles per second. Similarly, EXP100, the sparse experiment uses 3 point sources spaced about 100 km apart
147 along the axis of the wind (Figure 2, green crosses), with each source emitting 2.5×10^{17} particles per second. This
148 setup simulates a scenario with more sparsely distributed but much stronger increased localized emissions
149 compared to the other two experiments. A summary of the detailed configuration is listed in Table 2. It is also
150 important to note that these surface aerosol emission flux remain constant throughout the simulation, representing
151 a continuous aerosol spraying scenario over the region.



152

153 **Figure 2: Locations of aerosol emission source points with varying aerosol emission levels and spacing in three**
 154 **sensitivity experiments. Red dots indicate source points with 20 km spacing. Blue triangles are for source points with**
 155 **40 km spacing over upwind of domain. Green crosses represent source points with 100 km spacing upwind domain.**
 156 **Red line outlines the shape of interest area, Cairns Region, of this study.**

157 **Table 2: Details information of numerical experiments conducted in this study**

	Source Station #, spacing	Modifications
CTRL	0	N/A
EXP20	75, 20km	adding 1×10^{16} particles per second per station
EXP40	12, 40km	adding 6.25×10^{16} particles per second per station
EXP100	3, 100km	adding 2.5×10^{17} particles per second per station

158 **2.3 Observational Data**

159 Several observational datasets are used to evaluate the CTRL simulation. In this study, sounding data at 0000 UTC
 160 on 07 and 08 of February 2022 are obtained from the University of Wyoming upper-air sounding database for
 161 available station, Willis Island (code: 94299, Figure 1). Channel 13 brightness temperatures and RGB from
 162 Himwari-8 satellite dataset (Bureau of Meteorology, 2021) are obtained from the Australian Bureau of
 163 Meteorology for the time 0000 UTC on 07 and 08 of February 2022.

164 To evaluate the simulated cloud microphysical properties, we calculate the cloud droplet number concentration
 165 (CDNC) using Himawari-8 derived effective radius and cloud optical thickness obtained from the Australian
 166 Bureau of Meteorology (Bureau of Meteorology, 2022). Note that the cloud phase identification fails for some
 167 pixels, preventing subsequent microphysical retrievals (Figure S1). As result, the derived CDNC exhibits reduced
 168 cloud coverage compared to infrared brightness temperature. The equation used for calculating the CDNC is:



$$\text{CDNC} = \frac{2\sqrt{10}}{k\pi Q^3} \left[\frac{c_w \text{cot}}{\rho_l (r_{e,\text{top}})^5} \right]^{1/2},$$

169

170 where cot denotes the cloud optical thickness, and k is a parameter related to the dispersion of the assumed cloud
171 droplet size distribution; a constant value of 0.8 is used in this study. The scattering efficiency, Q, is set to its
172 geometric-optics limiting value of 2. The liquid water density, ρ_l , is taken as $1.0 \times 10^3 \text{ kg m}^{-3}$, and c_w represents
173 the temperature-dependent condensation rate (kg m^{-4}), prescribed as 80% of its adiabatic value following Bennartz
174 (2007). Although this 80% adiabatic assumption may introduce some temperature-dependent bias, its contribution
175 to the overall uncertainty is relatively small, as demonstrated by Huang et al. (2016). The effective radius, r_e , is
176 retrieved from Himawari-8 observations using the 1.6 μm channel. It should be noted that satellite-retrieved
177 effective radius represents conditions at a penetration depth below the cloud top that depends on the observation
178 wavelength. Compared to the 3.7 μm channel, the 1.6 μm channel penetrates approximately two to three times
179 deeper into the cloud, which can introduce a positive bias in the inferred CDNC and lead to uncertainties of up to
180 ~100% (Bennartz and Rausch, 2017; Huang et al., 2016).

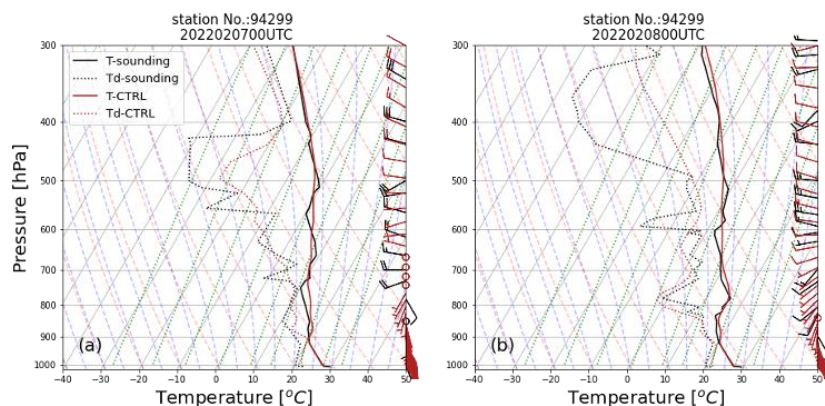
181 3 Results

182 3.1 Control simulation

183 The simulated synoptic and the cloud conditions are first evaluated by comparing the control simulation with
184 observations. The control simulation skilfully simulated the evolution of the synoptic-scale mean surface level
185 pressure and surface winds (not shown). Figure 3 shows the observed soundings (black) from Willis Island and
186 the simulated atmospheric profile (red) at the nearest grid point in the 1 km domain at 0000 UTC on 07 and 08
187 February. The simulated soundings at both times are in good agreement with observations, with both wind speed
188 and direction well captured throughout the profile.

189 Figure 4 compares the observed and simulated brightness temperature together with Himawari-8 true-color
190 imagery at 0000 UTC on 07 and 08 February 2022. The simulated brightness temperature is calculated using a
191 simplified approach, assuming unit surface emissivity and an effective cloud optical depth of one, and is therefore
192 intended solely for qualitative evaluation of the simulated cloud field. Overall, the cloud field is reasonably well
193 simulated in terms of the location and timing when compared against the Himawari-8 observation. While much
194 of the high-level cloud cover within the domain is underestimated or missing, resulting in imperfect alignment of
195 fine-scale cloud structures, the key features of maritime shallow clouds, visible in the true-color imagery, are
196 captured. These shallow cloud systems are the primary cloud regime of interest in this study, and their realistic
197 representation provides a reasonable basis for the subsequent analysis.

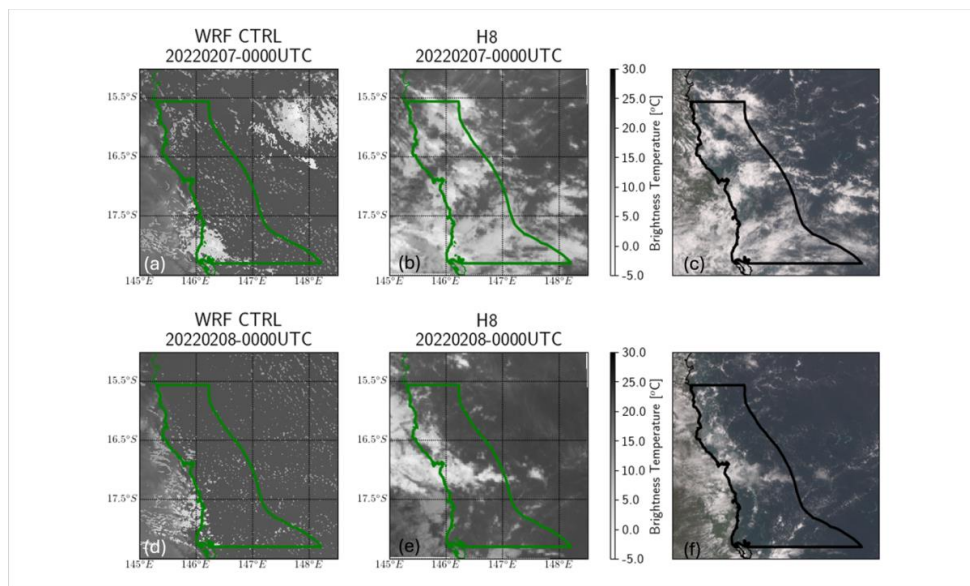
198 Figure 5 further compares the simulated cloud-top cloud droplet number concentration (CDNC) with Himawari-
199 8 derived CDNC at 0000 UTC on 07 and 08 February 2022. Overall, the simulated CDNC falls within a reasonable
200 quantitative range relative to the satellite-derived estimates. Some discrepancies persist, most notably a modest
201 negative bias in the CTRL simulation in localized regions and in areas affected by deeper or more heterogeneous
202 cloud systems. Given the large uncertainties inherent in satellite CDNC retrievals as mentioned earlier, these
203 differences are not unexpected and do not undermine the overall consistency. Despite these limitations, the overall
204 agreement supports the conclusion that the CTRL simulation reasonably captures the microphysical characteristics
205 of the target maritime shallow clouds, providing a strong foundation for the subsequent sensitivity analyses.



206

207 **Figure 3: (a) Comparison of the observed sounding profiles (black lines) from Willis Island (station No, 94299)**
 208 **alongside 1km WRF atmospheric profile simulations (red lines) from the nearest grid point on 07 of Feb 2022 at**
 209 **0000UTC. (b) same as (a), but for 08 of Feb 2022 at 0000UTC.**

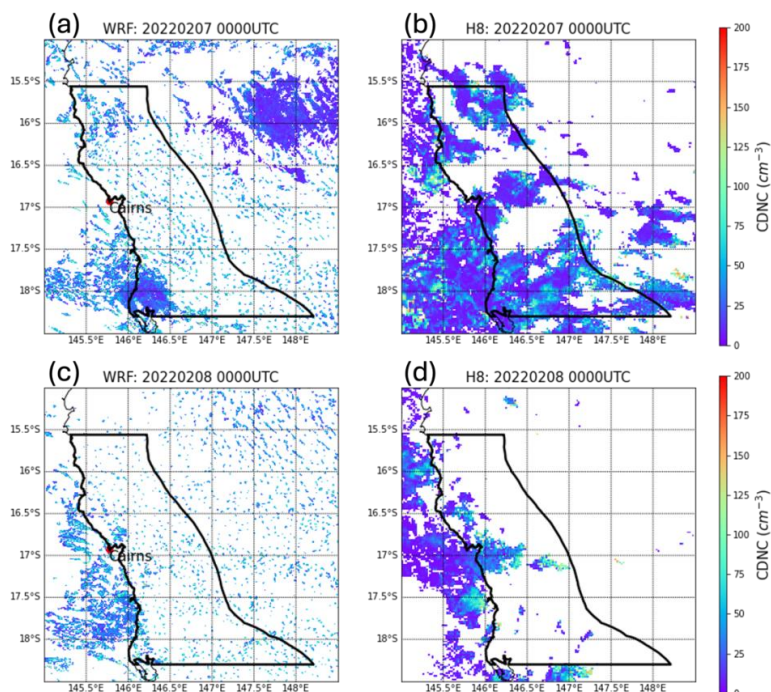
210



211

212 **Figure 4: (a) Simulated brightness temperatures from CTRL at 1km resolution on 07 of Feb 2022 at 0000 UTC. (b)**
 213 **Brightness temperatures of band 13 (10.4 μm) derived from Himawari-8 satellite observations on 07 of Feb 2022 at**
 214 **0000 UTC. Green lines outline the domain of Carins region. (c) True color image from Himawari-8 satellite**
 215 **observations on 07 of Feb 2022 at 0000 UTC. Black line outlines the domain of Carins region. Note that same color**
 216 **scales applied in (a) and (b). (d-f) same as (a-c), but for 08 of Feb 2022 at 0000 UTC.**

217



218

219 **Figure 5: (a) Simulated cloud droplet number concentration (CDNC) from CTRL at 1km resolution on 07 of Feb 2022**
 220 **at 0000 UTC. (b) Derived CDNC from Himawari-8 observations (at 1.6 μ m) on 07 of Feb 2022 at 0000 UTC. (c-d) same**
 221 **as (a-b), but for 08 of Feb 2022 at 0000 UTC. Note that same color scales applied in all panels.**

222 3.2 Aerosol distribution

223 Introducing continuous aerosol emissions in the three experiments leads to substantially elevated aerosol number
 224 concentrations over the Cairns region compared to the CTRL simulation. As shown in Figure 6a-c, all seeding
 225 scenarios produce a broad plume of enhanced aerosol spanning the target area, with peak increases on the order
 226 of several hundred per cubic centimeter near the source locations, confirming the effectiveness of the emission
 227 perturbations imposed in the experimental setups. Under prevailing southeasterly trade-wind conditions, a distinct
 228 downwind transport of aerosols is evident, characterized by a noticeable plume extending to the northwest from
 229 the source points in all sensitivity experiments.

230 In the EXP20 experiment, where source points are closely spaced (20 km apart), the downwind aerosol
 231 enhancements are spatially diffuse but broadly distributed, indicating a widespread influence. In the contrast,
 232 EXP100 experiment, with only three source points spacing 100 km apart, produces a higher peak aerosol
 233 concentration but with limited spatial coverage. EXP40 exhibited an intermediate structure, showing distinct
 234 plumes aligned along the prevailing wind trajectory.

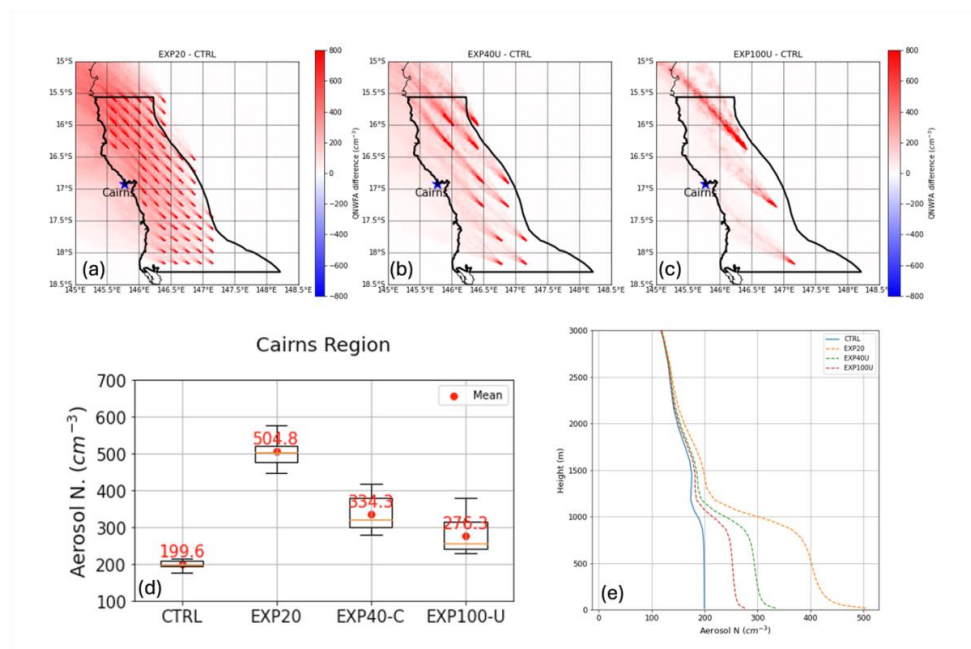
235 Looking over the Cairns region, the intensified surface aerosol emissions at the source points result in a noticeable
 236 increase in the domain-averaged surface aerosol number concentration (Figure 6d). This increase is more
 237 pronounced in EXP20 experiment, with domain-average increasing from 199.6 to 504.8 cm^{-3} . Smaller
 238 enhancements are obtained in EXP40 (334.3 cm^{-3}) and EXP100 (276.3 cm^{-3}), despite having identical total
 239 emissions. This behaviour arises because the aerosol scavenging and removal processes in the WRF Thompson
 240 aerosol-aware microphysics scheme are nonlinear with respect to the total aerosol number concentration (Wang
 241 et al., 2010; Weston et al., 2022). The precipitation scavenging efficiency increases approximately with the square



242 of total aerosol concentration. Consequently, in EXP100, local aerosol removal through self-scavenging is more
 243 effective, especially over the source points with high concentrated aerosol concentration, limiting the overall
 244 domain-mean enhancement. This demonstrates that source density exerts a stronger influence on the spatially
 245 averaged aerosol abundance than the emission rate at individual points. The closely spaced emitters in EXP20
 246 generate overlapping plumes that elevate background aerosol concentrations across a wider region, producing a
 247 more uniform and sustained enhancement. In contrast, the sparse, high-flux sources in EXP100 produce localized
 248 concentration maxima that dissipate more rapidly through scavenging removal, resulting in a smaller net increase
 249 in the total aerosol population across the domain.

250 The enhanced surface aerosol emission also leads to an increase in the atmospheric aerosol population, extending
 251 throughout the atmospheric boundary layer up to the inversion layer at around 1.5km (Figure 6e). This indicates
 252 that the added aerosols successfully penetrate the cloud layer, making them available to act as CCN in the
 253 numerous shallow cumuli present (cloud base in these cases is typically ~1 km). The sharp drop-off above ~2 km
 254 suggests the inversion capping the boundary layer (Figure 3) inhibits further lofting of aerosols into the free
 255 troposphere, which is expected for this shallow convective regime. The most substantial boundary-layer
 256 enhancement occurred in EXP20, consistent with its more homogeneous and spatially extensive surface plume.
 257 In contrast, EXP40 and EXP100 exhibited smaller domain-mean increases aloft, reflecting the greater spatial
 258 heterogeneity associated with their sparser emission distributions.

259 In summary, all aerosol-emission strategies substantially increased boundary-layer aerosol loading up the the top
 260 of the boundary layer over the GBR region, but the dense-source configuration (EXP20) achieved the most
 261 uniform and extensive enhancement, while the widely spaced configuration (EXP100) produced a more
 262 heterogeneous distribution characterized by strong local maxima and weaker domain-wise enrichment.



263

264 **Figure 6:** (a) Difference in surface aerosol number concentration between EXP20 and CTRL over the time period
 265 1600UTC on 06 Feb to 1600UTC on 08 Feb. (b) - (c) same as (a), but for difference between EXP40 and CTRL, EXP100
 266 and CTRL. Note that same color scale is applied to both (a) to (c). (d) Boxplot of area-averaged surface aerosol number
 267 concentration over Cairns Region throughout the simulation time. Red dots represent the mean values from each
 268 experiment. (e) Vertical profiles of time-area-averaged aerosol number concentration over Cairns Region throughout
 269 the simulation time.



270

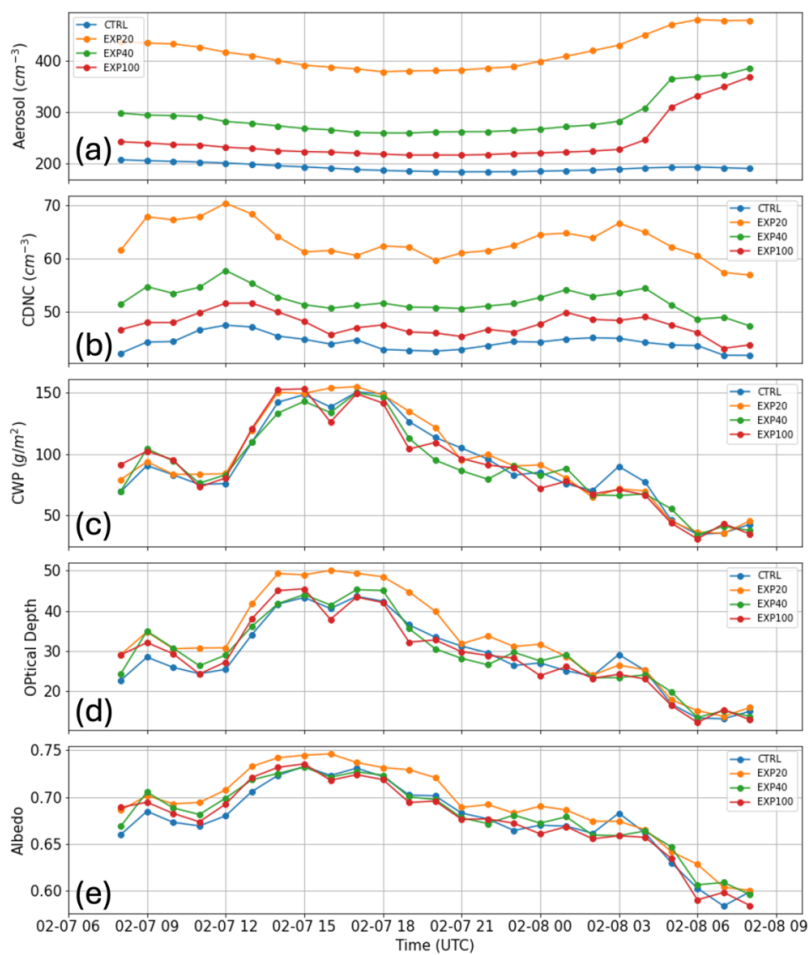
271 3.3 Cloud properties responses

272 Given the evolution of cloud systems during the simulation period, the analysis in this study focuses on the 24-
273 hour period from 08 UTC 07 February to 08 UTC 08 February, when the domain was predominantly characterized
274 by shallow stratocumulus cloud regimes (Figure S2). This regime is selected as it represents the most relevant
275 condition for assessing the potential of MCB.

276 The imposed aerosol perturbations lead to notable modifications in cloud microphysical and, to a lesser extent,
277 macrophysical properties over the Cairns region. As shown in Figure 7b and Figure 8b, cloud droplet number
278 concentration (CDNC) exhibits the strongest and most consistent response to aerosol injections, with all sensitivity
279 experiments showing substantial enhancements relative to the CTRL simulation. As expected, increased CCN
280 availability resulted in clouds containing a greater number of smaller droplets. In EXP20, the domain-mean CDNC
281 increased by approximately 72.7% relative to CTRL, whereas EXP40 and EXP100 displayed more moderate yet
282 significant increases of ~32.3% and ~13.9%, respectively. These responses correspond closely with the magnitude
283 of aerosol enhancement achieved in each experiment (Figure 7a and Figure 8a), with EXP20 exhibiting the highest
284 aerosol loading and, consequently, the largest increase in droplet number concentration.

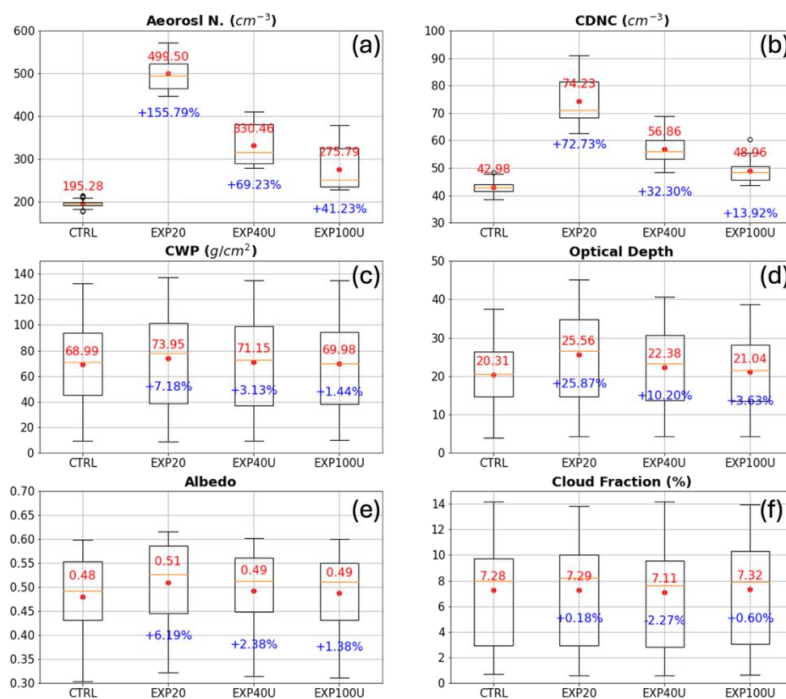
285 Despite the substantial increase in CDNC, the corresponding changes in cloud water path (CWP) are
286 comparatively modest. In EXP20, the domain-averaged CWP is approximately 7.2% higher than in CTRL (Figure
287 5c). The EXP40 and EXP100 exhibit even smaller increases of 3.13% and 1.44% respectively relative to CTRL.
288 These subdued CWP responses, relative to the pronounced CDNC enhancements, indicate that increasing aerosol
289 loading did not substantially thicken the clouds in terms of column integrated liquid water content. Moreover, the
290 CWP response displays a pronounced nonlinear and temporally variable behaviour (Figure 7c), with periods of
291 enhanced CWP coinciding with elevated aerosol concentrations, interspersed with intervals where the seeded
292 experiments show reduced CWP relative to CTRL. This variability suggests that the influence of aerosol
293 perturbations on cloud water is strongly modulated by fluctuations in meteorological conditions and boundary-
294 layer dynamics during the simulation period, which will be examined in the next section.

295 Similarly, changes in cloud fraction (CF) are minimal. Note that, in the WRF output, CF for each grid point is
296 given by either binary number 1 or 0 to indicate either cloudy or cloud free pixel. In this study, CF of Cairn region
297 is defined as the proportion of total grid points in the domain that are classified as cloudy grids. As shown in
298 Figure 8f, the domain-averaged CF remains nearly constant across all experiments, with mean values around 7%
299 and differences of less than 2% relative to CTRL. These responses can be considered negligible in the context of
300 domain-mean variability. In other words, cloud coverage responds only weakly to changes in aerosol loading as
301 represented in this model configuration. Consequently, the lack of a discernible CF response suggests that radiative
302 forcing induced by MCB in this case would primarily arise from modifications in cloud optical properties, rather
303 than from changes in cloud amount.



304

305 Figure 7: Time series of domain-averaged (a) surface aerosol number concentration, (b) CDNC, (c) cloud water path,
306 (d) optical depth, and (4) synthetic cloud albedo over the Cairns Region. Note that all variables are averaged over
307 cloudy grid points. Shaded intervals denote nighttime locally.



308

309 **Figure 8: Boxplots of aerosol and cloud properties over Cairns Region from CTRL and sensitivity experiments. Time**
 310 **period for analysis is 08UTC 07 Feb to 08 UTC 08 Feb 2022. Red numbers are mean values of each experiment, and**
 311 **blue numbers are differences with respect to CTRL experiment.**

312 The cloud optical depth and albedo are therefore further diagnosed to quantify the radiative effects of the aerosol-
 313 induced microphysical changes. Following prior studies (Zhang et al., 2005), the cloud optical depth (τ) is
 314 estimated from the simulated CWP and CDNC using an approximate relationship for warm clouds:

$$315 \quad \tau = 0.19 (\text{CWP})^{5/6} (N_c)^{1/3},$$

316 where CWP is in kg m⁻² and N_c is cloud droplet number concentration in cm⁻³. This formula captures the first-
 317 order dependence of τ on both cloud water amount and droplet number (Twomey, 1977), and is reasonably
 318 accurate for shallow cloud regimes (Zhang et al., 2005). The cloud albedo (A) is then computed from τ using the
 319 approximate analytic expression:

$$320 \quad A = \frac{\tau}{\tau + 6.8} \text{ (Seifert and Heus, 2013; after Twomey, 1977),}$$

321 Despite the relatively modest changes in CWP, the cloud optical depth (τ) and albedo (A) exhibit pronounced
 322 increases (Figure 8d-e), especially in EXP20, reflecting the strong microphysical sensitivity to aerosol
 323 perturbations. In EXP20, the domain-mean τ increases by approximately 25.9%, accompanied by a 6.2%
 324 enhancement in cloud albedo, driven primarily by the substantial increase in CDNC. These changes indicate
 325 brighter and more reflective clouds, thereby enhancing the potential to reduce surface shortwave radiation through
 326 the Twomey effect. Smaller but consistent albedo increases are observed in the other experiments: EXP40 yields
 327 an enhancement of roughly 10% in τ and 3% in A , while EXP100 shows a modest 1–3% increases in optical
 328 properties relative to CTRL. Although these optical properties changes appear moderate in absolute terms, they
 329 are climatically significant, being comparable in magnitude to the estimated radiative feedback strength of
 330 subtropical marine low clouds reported in recent observational and modeling studies (e.g., Wood, 2012; Seifert et
 331 al., 2015).

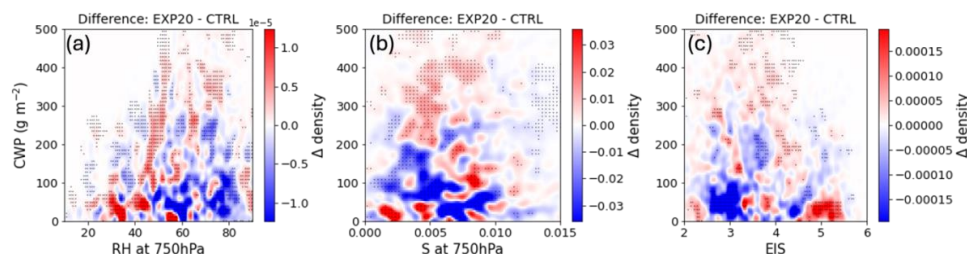


332 In summary, the microphysical effects of aerosol perturbation are clearly evident, whereas the macrophysical
 333 cloud properties (CWP and cloud fraction) show weak or no response on average in these simulations. This
 334 contrast demonstrates the potential nonlinear nature of cloud–aerosol interactions. The dominant response
 335 observed in these cases is the Twomey effect (increased reflectance via droplet number), with little support for a
 336 strong Albrecht effect (increased cloud water or coverage via precipitation suppression) under these conditions.
 337 The magnitude and sign of these optical and radiative responses, however, are not uniform throughout the
 338 simulation period. Temporal variability in both CWP and albedo suggests that the efficiency of aerosol–cloud
 339 interactions is strongly modulated by the background meteorological state. Factors such as relative humidity,
 340 lower-tropospheric stability, and wind shear influence the extent to which aerosol-induced microphysical
 341 adjustments translate into macroscopic or radiative effects. The following section examines how variations in
 342 these environmental parameters govern the observed differences in cloud responses across the sensitivity
 343 experiments.

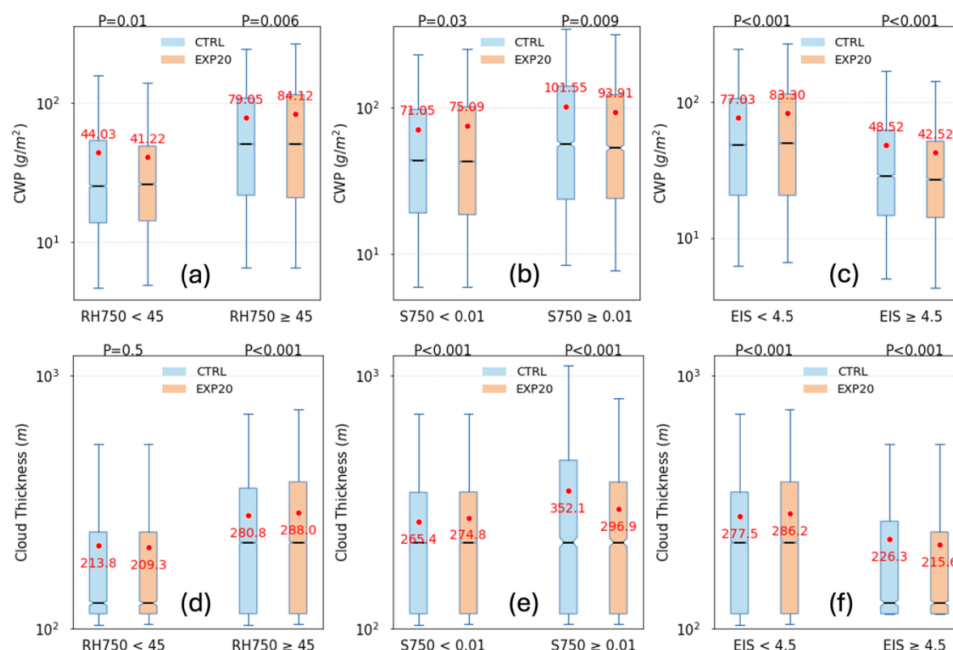
344 3.4 The impact of meteorology

345 The variations identified in CWP responses to aerosol injections motivated an examination of the background
 346 meteorological factors that might modulate cloud–aerosol interactions. Three key parameters are considered: mid-
 347 level relative humidity (RH) at 750 hPa, representing moisture conditions above cloud tops, vertical wind shear
 348 (S) at 750 hPa, defined as the magnitude of the horizontal wind vector change across the cloud layer (calculated
 349 as $\frac{\sqrt{\Delta u^2 + \Delta v^2}}{\Delta z}$), and the estimated inversion strength (EIS), which quantifies lower-tropospheric stability following
 350 the formulation of Wood and Bretherton (2006). These parameters have been shown to strongly influence cloud-
 351 top drying, entrainment, and evaporative processes in marine stratocumulus and cumulus regimes (Gryspeerd et
 352 al., 2019; Mauger and Norris, 2010; Bretherton et al., 2007; 2019), and therefore provide a physically meaningful
 353 framework for interpreting the environmental dependence of the modelled cloud responses. It is important to note
 354 that, in this section, the analysis focuses on EXP20 and CTRL as representative cases. The other two sensitivity
 355 experiments (EXP40 and EXP100) exhibit weaker yet qualitatively consistent responses with those of EXP20,
 356 supporting the robustness of the identified relationships.

357



358 **Figure 9: Joint distribution analysis of cloud water response under different environmental conditions. Panels show**
 359 **the difference in 2D frequency (EXP20-CTRL) as colored contours. (a) Frequency of occurrence of RH at 750 hPa and**
 360 **CWP pairs. (b) same (a), but for S at 750 hPa and CWP pairs. (c) same as (a), but for pairs of EIS and CWP. Note that**
 361 **colours with black dots indicate significant differences.**



362

363 **Figure 10: Boxplots of cloud water path (CWP) in CTRL (blue) and EXP20 (orange), categorized by meteorological**
 364 **conditions. (a) CWP under two ranges of 750 hPa relative humidity: low (<45%), and high (≥45%). (b) Same as (a)**
 365 **but stratified by wind shear (S) at 750 hPa: weak ($S < 0.01 \text{ s}^{-1}$), strong ($\geq 0.01 \text{ s}^{-1}$). (c) Stratified by inversion strength**
 366 **EIS: weakly capped ($EIS < 4.5 \text{ K}$), strongly capped ($EIS \geq 4.5 \text{ K}$). Red dots indicate the average values of each category.**
 367 **Significant test results (P values) are shown above each category. (d-f) same as (a-c), but for comparison of cloud**
 368 **thickness in CTRL (blue) and EXP20 (orange).**

369 As shown in Figure 9a, under relatively high humidity conditions (e.g. $RH \geq 45\%$) at 750 hPa, the EXP20
 370 experiment exhibits a greater number of grid points with higher CWP compared to CTRL, reflected, for example,
 371 by an increased frequency of grid points with CWP around 300 g m^{-2} . Conversely, under low humidity conditions
 372 (e.g. RH_{750} less than 45%), EXP20 shows reduced CWP relative to CTRL, indicating a humidity-dependent
 373 response to aerosol perturbations. This relationship is further quantified in Figure 10a, where CWP is categorized
 374 by mid-level relative humidity, with the 45% RH_{750} threshold selected based on the regime separation evident in
 375 Figure 9a. Note that Student's t-tests are performed for each humidity category to assess the statistical significance
 376 of the differences in mean CWP between the two experiments. When RH_{750} exceeds approximately 45%, mean
 377 CWP in CTRL increases from 79.05 to 84.32 g m^{-2} with P value of 0.006, reflecting the significant positive
 378 influence of a moister free troposphere on cloud water retention. In contrast, under the low humidity conditions
 379 ($RH_{750} < 45\%$), EXP20 displays a slight reduction in CWP despite elevated aerosol concentrations. These results
 380 suggest that a moist free troposphere enhances the likelihood of increased cloud water in response to aerosol
 381 loading, whereas a moist free troposphere promotes entrainment-driven drying and limits cloud thickening, leading
 382 to reduced CWP in the seeded case. This result is physically consistent with the mechanism proposed by Ackerman
 383 et al. (2004), in dry conditions, aerosol-induced suppression of drizzle can enhance cloud-top evaporation (via
 384 increased entrainment of dry air), offsetting any gain in liquid water from reduced rainfall. But in humid conditions
 385 aloft, entrained air is less drying, so the clouds can retain more water when drizzle is suppressed, thus CWP
 386 increases.

387 A similar analysis for S at 750 hPa (Figure 9b and Figure 10b) reveals a clear dynamical modulation of the aerosol–
 388 cloud relationship. Under weak shear above cloud top ($S < 0.01 \text{ s}^{-1}$), the aerosol-seeded clouds in EXP20 exhibit
 389 higher CWP than those in CTRL, whereas under strong shear conditions ($S \geq 0.01 \text{ s}^{-1}$), EXP20 clouds show a



390 marked reduction in CWP relative to CTRL. Statistically, the mean CWP in EXP20 increases from 71.05 g m⁻² to
391 75.09 g m⁻² (P = 0.03) under low shear environments, but becomes noticeably (P = 0.009) lower than CTRL when
392 wind shear intensifies. This behaviour suggests that strong vertical shear disrupts and tilts convective updrafts,
393 enhances turbulent mixing, and promotes entrainment of dry air from above the cloud layer, with these being
394 counteract the microphysical thickening effect induced by aerosol loading. In contrast, under weak shear
395 conditions, clouds remain more vertically coherent and can deepen more effectively, allowing aerosol-induced
396 microphysical adjustments to manifest as increased cloud water.

397 Finally, the dependence of CWP on lower-tropospheric stability, expressed through the estimated inversion
398 strength (EIS), is illustrated in Figure 9c and Figure 10c. Under low-stability conditions (EIS < 4.5 K), indicative
399 of a weak or absent inversion capping the boundary layer, aerosol perturbation leads to an increase in CWP from
400 77.03 to 82.15 g m⁻² significantly (P < 0.001). In contrast, under high-stability conditions (EIS ≥ 4.5 K), where a
401 strong inversion limits vertical development, the seeded clouds exhibit reduced CWP (43.33 g m⁻²) compared to
402 48.52 g m⁻² in CTRL. A strong inversion confines cloud growth, producing thinner and more stratified layers that
403 are highly susceptible to entrainment drying. Conversely, when the inversion is weak, clouds can deepen and
404 become more dynamically active. In such environments, the presence of additional CCN delays precipitation onset,
405 allowing greater liquid water retention. This interpretation is further supported by the analysis of cloud thickness
406 stratified by meteorological conditions. As shown in Figure 10d–f, significantly increased cloud thickness is seen
407 under high humidity, lower wind shear at 750 hPa, and low EIS conditions. Note that the cloud thickness in the
408 model simulation is defined using a threshold cloud water mixing ratio of 10⁻⁶ kg kg⁻¹, consistent with similar
409 cloud mask criteria employed in previous WRF studies (Arbizu-Barrena et al., 2015). Overall, these results
410 indicate that a moist, weakly capped atmosphere favours positive cloud water responses to aerosol perturbations,
411 whereas a dry, strongly capped environment suppresses them.

412 These analyses demonstrate that the cloud water response to aerosol perturbations is strongly conditioned by the
413 prevailing meteorological environment. A moist, weakly sheared, and weakly capped boundary layer favours
414 positive CWP responses to aerosol enhancement, facilitating cloud deepening and greater liquid water growth.
415 Conversely, dry, strongly sheared, and stably stratified conditions suppress this response by promoting
416 entrainment-driven evaporation and inhibiting vertical cloud growth. These findings highlight the regime-
417 dependent nature of aerosol–cloud interactions, underscoring that the efficacy of MCB over the GBR is highly
418 sensitive to the large-scale thermodynamic and dynamic state of the atmosphere. Consequently, identifying and
419 targeting favourable meteorological conditions is also critical for maximizing the radiative benefit of MCB
420 interventions.



421 **4 Conclusions and Discussions**

422 Using convection-permitting WRF simulations with the Thompson aerosol-aware microphysics scheme, this
423 study examined how spatial variability in aerosol emissions influences the microphysical, macrophysical, and
424 radiative properties of shallow marine clouds over the GBR. Three sensitivity experiments were conducted in
425 which the total aerosol emission was held constant but the number and spacing of source points varied.

426 The key findings are summarized below:

- 427 • Densely spaced emission sources (EXP20) produced more homogeneous and widespread increases in
428 boundary-layer aerosol concentrations. In contrast, sparsely distributed sources generated localized peaks
429 in aerosol concentration that were efficiently scavenged, leading to smaller domain-mean increases,
430 despite identical total aerosol emissions.
- 431 • Strong responses in CDNC and cloud optical depth, yielding brighter clouds and higher mean albedo
432 with additional aerosol perturbations. Despite these pronounced microphysical changes, responses in
433 CWP and CF were modest, consistent with a regime in which the Twomey effect dominates, while the
434 Albrecht effect remains weak.
- 435 • Positive CWP responses were favoured in environments characterized by high mid-level humidity, weak
436 wind shear, and weak lower-tropospheric stability. Conversely, dry, strongly sheared, and stably stratified
437 conditions led to reductions in CWP despite elevated aerosol levels.
- 438 • The potential for marine cloud brightening over the GBR depends not only on aerosol loading
439 configurations but also on meteorological controls. Optimal outcomes occur when seeding coincides with
440 favourable thermodynamic conditions.

441 The findings confirm that radiative forcing can be meaningfully enhanced under suitable conditions through
442 spatially coherent aerosol seeding. As such, strategic deployment of MCB during favorable weather regimes holds
443 promise as a targeted intervention to mitigate extreme heat exposure over sensitive marine ecosystems like the
444 GBR. From a radiative forcing perspective, substantial increases in cloud albedo, as demonstrated in this study,
445 can be achieved primarily through microphysical adjustments, even in the absence of significant changes in cloud
446 macrophysical structure. The dominant mechanism of radiative modulation in our simulations was the Twomey
447 effect, whereby increased aerosol concentrations enhanced cloud droplet number and optical depth. The shallow
448 clouds in our case produced very light precipitation (mean rain rates $\leq 0.01 \text{ mm h}^{-1}$; see Figure S3), thereby
449 limiting the aerosol–precipitation interactions, such as rain suppression. This result further confirms the findings
450 from idealised large-eddy simulations by Seifert et al. (2015), which showed that aerosol–cloud interactions are
451 largely governed by the Twomey effect under non- or weakly precipitating conditions. Correspondingly, variations
452 in liquid water path and cloud fraction remain comparatively small. In the EXP20 experiment, a $\sim 25\%$ increase
453 in optical depth led to a $\sim 6\%$ absolute increase in synthetic cloud albedo. While modest in absolute terms, such
454 an enhancement translates into a non-negligible reduction in surface shortwave flux, potentially on the order of
455 several tens of W m^{-2} (Alinaghi et al., 2024) under typical daytime conditions. If sustained over multi-days to
456 weeks timescales, this reduction could lower sea surface temperatures by a fraction of a degree Celsius, an effect
457 that previous studies suggest may be sufficient to mitigate the severity or onset of coral bleaching events (Harrison
458 et al., 2019). However, the lack of corresponding increases in cloud fraction indicates that this enhanced reflection
459 is confined to the pre-existing cloud-covered portion of the sky in the conditions modeled, limiting the area extent
460 of radiative cooling. Furthermore, the present study did not explicitly account for the direct radiative effects of
461 aerosols due to the limitations of the bulk aerosol-aware microphysics scheme used. To more fully quantify the
462 total radiative impact of aerosol injection scenarios, future studies should incorporate fully coupled aerosol–
463 chemistry–radiation interactions using models such as WRF-Chem or other chemically-resolving frameworks.

464 The CWP responses to aerosol perturbations, as indicated in this study, showed dependence to the background
465 meteorological states. Over the GBR, in “favorable” conditions (high moisture aloft, weak inversion and wind
466 shear), we observed that additional aerosols lead to increases in cloud water and thickening of the cloud layer,
467 indicating the most positive outcome for reflectivity. Whereas, in “unfavorable” conditions (dry aloft, strong
468 inversion, high shear), adding aerosols made clouds more susceptible to evaporation and in some instances
469 reduced the total cloud water. These results align with prior studies of stratocumulus decks which found that



470 aerosol perturbations can either deepen clouds or thin them, contingent on above-cloud humidity (Ackerman et
471 al., 2004). Our work extends this understanding to shallow maritime cumulus, emphasizing that MCB will be
472 most efficient when timed with supportive weather regimes. This has important implications for designing
473 effective MCB interventions. The same aerosol seeding strategy can have markedly different outcomes depending
474 on ambient humidity, stability, and winds. Furthermore, our results show that CDNC exhibits a consistently linear
475 enhancement with increasing aerosol perturbations over the GBR, largely independent of the meteorological
476 background, indicating a robust direct microphysical response. These are in line with a growing body of literature
477 suggesting that the radiative cooling from aerosol–cloud interactions is often driven by droplet concentration
478 changes, while cloud water path adjustments are buffered by meteorological factors (Rosenfeld et al., 2019;
479 Gryspeerdt et al., 2019; Feingold et al., 2010).

480 In terms of MCB efficiency, the spatial configuration of aerosol sources plays a critical role in determining the
481 effectiveness of aerosol delivery and subsequent cloud modification. The widely distributed emission scenario
482 (EXP20) resulted in a more homogeneous and persistent increase in atmospheric aerosol concentrations compared
483 to the more sparsely spaced, high-flux emission case (EXP100), despite all experiments having the same total
484 aerosol mass flux. This outcome highlights that denser spatial coverage can compensate for lower per-source
485 emission intensity by facilitating plume overlap and minimizing gaps between seeded regions. In contrast, the
486 concentrated high-emission sources in EXP100 experienced more localized scavenging, particularly near the
487 source points, which led to more rapid aerosol removal and ultimately smaller net increases in cloud condensation
488 nuclei (CCN) across the domain. This outcome aligns with prior modeling work (e.g., Wang et al., 2011; Possner
489 et al., 2018) indicating that the effectiveness of MCB is strongly influenced by the balance between aerosol
490 injection, transport, and removal processes, especially in marine environments where wet scavenging dominates.
491 Moreover, our results underscore that aerosol injection efficiency does not scale linearly with emission intensity.
492 Instead, spatial and temporal coherence in seeding appears to enhance domain-mean radiative forcing more
493 effectively, which is consistent with earlier sensitivity studies in stratocumulus regions (e.g., Latham et al., 2008).
494 Our work reinforces the importance of designing MCB interventions with sufficient spatial coherence to maximize
495 aerosol utilization and domain-wide radiative impact.

496 While the findings presented here advance process-level understanding, several limitations should be
497 acknowledged. The results presented in this study are derived from a limited set of simulations representing a
498 particular meteorological period over the GBR region. Although this case was selected as representative of typical
499 summer trade-wind conditions, it does not encompass the full diversity of weather regimes that occur across the
500 region during the summer season (Richards et al., 2024). The cloud responses to aerosol perturbations may vary
501 substantially under different synoptic conditions or convective environments. A broader ensemble of simulations,
502 spanning the entire coral bleaching season (January–April; Zhao et al., 2021) and a range of meteorological
503 regimes, would be needed to develop more robust and generalizable conclusions regarding the efficacy of MCB
504 over the GBR. Additionally, our simulations ran for only three days on a relatively small domain. This setup
505 captures the direct local effects of aerosol on clouds (the “first indirect effect” and microphysical feedbacks) but
506 cannot account for longer-term or larger-scale feedbacks. For instance, any changes in cloud radiative forcing
507 could eventually alter surface heat fluxes, pressure, and winds, which might feed back onto cloud formation, a
508 process requiring a larger domain, longer simulations, and coupled ocean–atmosphere model to explore.
509 Furthermore, the shallow clouds in our case produced very light precipitation. Consequently, aerosol–precipitation
510 interactions, such as rain suppression, were weak in the present case. In environments characterized by more
511 vigorous precipitation (e.g., deeper cumulus or stratocumulus-to-cumulus transition regimes or exceptionally
512 clean aerosol regimes), aerosol seeding may exert a stronger influence through the second indirect effect (Albrecht,
513 1989). Future work should examine aerosol impacts under a wider range of precipitation efficiencies to determine
514 whether the mixed CWP responses identified here persist across different cloud regimes. Nevertheless, the
515 findings presented here provide an important first step toward understanding how the spatial distribution of aerosol
516 emissions influences cloud microphysical and radiative responses over the GBR. By explicitly resolving cloud–
517 aerosol interactions under convection-permitting resolution, this study highlights the nonlinear sensitivity of cloud
518 albedo enhancement to emission spacing and local meteorological conditions. These results underscore that the
519 efficacy of MCB is not only governed by aerosol loading but also critically dependent on source configuration



520 and ambient atmospheric state. Such insights are essential for the design and optimization of future MCB field
521 trials and for assessing their potential climatic benefit in mitigating thermal stress over coral reef ecosystems.
522 Looking ahead, validation of modeled cloud responses with in-situ and remote sensing observations will be
523 essential. Field campaigns involving aircraft-based measurements (e.g., Hernandez-Jaramillo et al., 2024) can
524 provide valuable data on CDNC, LWP, and aerosol characteristics during seeding experiments. Integrating
525 atmospheric simulations with ocean models would further enable quantification of downstream impacts on sea
526 surface temperatures and coral bleaching risk. In summary, this study provides new insight into how aerosol
527 emission geometry and meteorology jointly regulate the effectiveness of marine cloud brightening in shallow
528 cumulus environments. Continued observational and modeling work is essential to evaluate the feasibility, risks,
529 and climatic implications of such geoengineering approaches in practice.



530 **Acknowledgements:** This work is supported by Reef Restoration and Adaptation Program which is funded by
531 the partnership between the Australian Governments Reef Trust and the Great Barrier Reef foundation. The
532 Australian National Computational Infrastructure is thanked for providing the computational resources. The
533 authors would like to acknowledge the Traditional Owners of the Great Barrier Reef, particularly the Wulgurukaba
534 and Bindal people of the Townsville region nearby the area of our case study.

535 **Author contribution:** W.Z., Y.H., S.S. and D.H. developed the ideas and designed the study. W.Z. collected the
536 data, performed the analysis and prepared the draft manuscript. Y.H., S.S., and D.H. supervised and reviewed the
537 manuscript. All authors made substantial contributions to this work and approved the final version of the
538 manuscript.

539 **Competing Interests:** At least one of the (co-)authors is a member of the editorial board of Atmospheric
540 Chemistry and Physics.

541 **Data availability statement:** All data sets used in this study are freely and publicly available online and may be
542 accessed directly as follows. The University of Wyoming upper-air sounding is downloaded from
543 <http://weather.uwyo.edu/upperair/sounding.html>. The ERA5 reanalysis data is available at the website:
544 <https://cds.climate.copernicus.eu/cdsapp#!/search?-type=dataset>. The Himawari-8 full disk observational
545 products are available at NCI THREDDS Data Server: [https://dapds00.nci.org.au/thredds/catalogs/ra22/satellite-](https://dapds00.nci.org.au/thredds/catalogs/ra22/satellite-products/arc/obs/himawari-ahi/fldk/fldk.html)
546 [products/arc/obs/himawari-ahi/fldk/fldk.html](https://dapds00.nci.org.au/thredds/catalogs/ra22/satellite-products/arc/obs/himawari-ahi/fldk/fldk.html). The Himawari-8 true color imagery and cloud types classification
547 are available at JAXA Himawari Monitor supplied by P-Tree System: <https://www.eorc.jaxa.jp/ptree/>.



548 **References**

- 549 Australian Institute of Marine Science (AIMS): Coral Bleaching Events. [https://www.aims.gov.au/research-](https://www.aims.gov.au/research-topics/environmental-issues/coral-bleaching/coral-bleaching-events)
550 [topics/environmental-issues/coral-bleaching/coral-bleaching-events](https://www.aims.gov.au/research-topics/environmental-issues/coral-bleaching/coral-bleaching-events), last accessed: 02/02/2026, 2026.
- 551 Ackerman, A. S., Kirkpatrick, M. P., Stevens, D. E., and Toon, O. B.: The impact of humidity above stratiform
552 clouds on indirect aerosol climate forcing. *Nature*, 432(7020), 1014-1017, 2004
- 553 Albrecht, B. A.: Aerosols, cloud microphysics, and fractional cloudiness. *Science*, 245(4923), 1227–1230.
554 <https://doi.org/10.1126/science.245.4923.1227>, 1989.
- 555 Alinaghi, P., Janssens, M., Choudhury, G., Goren, T., Siebesma, A. P., and Glassmeier, F.: Shallow cumulus cloud
556 fields are optically thicker when they are more clustered. *Quarterly Journal of the Royal Meteorological*
557 *Society*, 150(763), 3566-3577, 2024
- 558 Arbizu-Barrena, C., Pozo-Vázquez, D., Ruiz-Arias, J. A., and Tovar-Pescador, J. Macroscopic: cloud properties
559 in the WRF NWP model: An assessment using sky camera and ceilometer data. *Journal of Geophysical*
560 *Research: Atmospheres*, 120(19), 10-297, 2015.
- 561 Ahlm, L., Jones, A., Stjern, C. W., Muri, H., Kravitz, B., and Kristjánsson, J. E.: Marine cloud brightening—as
562 effective without clouds. *Atmospheric Chemistry and Physics*, 17(21), 13071-13087, 2017.
- 563 Baresi, U., Baum, C.M., Fischer, T.B., Lockie, S., Piggott-McKellar, A., Graham, V., Bohensky, E., Fritz, L.B.,
564 Shumway, N., Harrison, D.P., Foster, R., Sovacool B.K., Vella K., and Ristovski Z.: A call for strategic
565 assessments of regional applications of solar radiation management: Exploring the challenges and
566 opportunities from marine cloud brightening and albedo surface modification. *Environmental impact*
567 *assessment review*, 110, 107701, 2025.
- 568 Bennartz, R.: Global assessment of marine boundary layer cloud droplet number concentration from satellite. *J.*
569 *Geophys. Res.*, 112, D02201, doi:10.1029/2006JD007547, 2007.
- 570 Braga, R. C., Rosenfeld, D., Hernandez, D., Medcraft, C., Efraim, A., Moser, M., Lucke J., Doss A., and Harrison,
571 D.: Cloud processing dominates the vertical profiles of aerosols in marine air masses over the Great
572 Barrier Reef. *Atmospheric research*, 315, 107928, 2025.
- 573 Bretherton, C. S., Blossey, P. N., and Uchida, J.: Cloud droplet sedimentation, entrainment efficiency, and
574 subtropical stratocumulus albedo. *Geophysical research letters*, 34(3), 2007.
- 575 Bretherton, C. S., McCoy, I. L., Mohrmann, J., Wood, R., Ghate, V., Gettelman, A., Bardeen C.G., Albrecht B.A.,
576 and Zuidema, P.: Cloud, aerosol, and boundary layer structure across the Northeast Pacific
577 stratocumulus–cumulus transition as observed during CSET. *Monthly weather review*, 147(6), 2083-
578 2103, 2019.
- 579 Bureau Of Meteorology: Bureau of Meteorology Satellite Observations (Collection). NCI Australia.
580 <https://doi.org/10.25914/61A609F9E7FFA>, 2021.
- 581 Bureau Of Meteorology: Bureau of Meteorology Satellite Derived Products (Collection). NCI Australia.
582 <https://dx.doi.org/10.25914/5QRS-QB54>, 2022.
- 583 Chen, F., and J. Dudhia: Coupling an advanced landsurface/hydrology model with the Penn State/NCAR MM5
584 modeling system. Part I: Model description and implementation. *Mon. Wea. Rev.*, 129, 569–585, doi:
585 10.1175/1520-0493(2001)1292.0.CO;2, 2001.
- 586 Colarco, P., A. da Silva, M. Chin, and T. Diehl: Online simulations of global aerosol distributions in the NASA
587 GEOS-4 model and comparisons to satellite and ground-based aerosol optical depth. *J. Geophys. Res.*,
588 115, D14207, doi:10.1029/2009JD012820, 2010.



- 589 Condie, S.A., Anthony, K., Babcock, R.C., Baird, M.E., Beeden, R., Fletcher, C.S., Gorton, R., Harrison, D.,
590 Hobday, A.J., Plagányi, É.E. and Westcott, D.A.: Large-scale interventions may delay decline of the
591 Great Barrier Reef. *Royal Society Open Science*, 8(4), 201296, 2021.
- 592 Dagan, G., Koren, I., Altaratz, O., and Heiblum, R. H.: Aerosol effect on the evolution of the thermodynamic
593 properties of warm convective cloud fields. *Scientific reports*, 6(1), 38769, 2016.
- 594 Feingold, G., Koren, I., Wang, H., Xue, H., and Brewer, W. A.: Precipitation-generated oscillations in open cellular
595 cloud fields. *Nature*, 466(7308), 849-852, 2010.
- 596 Gryspeerdt, E., Goren, T., Sourdeval, O., Quaas, J., Mülmenstädt, J., Dipu, S., Unglaub, C., Gettelman, A. and
597 Christensen, M.: Constraining the aerosol influence on cloud liquid water path. *Atmospheric Chemistry
598 and Physics*, 19(8), pp.5331-5347, 2019.
- 599 Harrison, D. P.: An overview of environmental engineering methods for reducing coral bleaching stress.
600 *Oceanographic processes of coral reefs*, 403-418, 2024.
- 601 Harrison DP, Harrison L, Baird M, Utembe S, Schofield R, Escobar Correa R, Mongin M, Rizwi F.:
602 T14: Environmental Modelling of Large Scale Solar Radiation Management. A report provided to the
603 Australian Government from the Reef Restoration and Adaptation Program. RRAP.
604 <https://gbrrestoration.org/resources/reports/>, 2019.
- 605 Harrison, L. P., Medcraft, C., and Harrison, D.: Effervescent nozzle design to enable outdoor marine cloud
606 brightening experimentation. *Environmental Science: Atmospheres*, 2025.
- 607 Harrison, D. P.: Could ‘marine cloud brightening’ reduce coral bleaching on the Great Barrier Reef?. *The
608 Conversation*, 2023.
- 609 Hersbach, H., de Rosnay, P., Bell, B., Schepers, D., Simmons, A., Soci, C., Abdalla, S., Alonso-Balmaseda, M.,
610 Balsamo, G., Bechtold, P. and Berrisford, P.: Operational global reanalysis: Progress, future directions
611 and synergies with NWP. *ECMWF ERA Report Series*, 27, 65, doi: 10.21957/tkic6g3wm, 2018.
- 612 Hersbach, H., Bell, B., Berrisford, P., Hirahara, S., Horányi, A., Muñoz-Sabater, J., Nicolas, J., Peubey, C., Radu,
613 R., Schepers, D. and Simmons, A.: The ERA5 global reanalysis. *Quarterly Journal of the Royal
614 Meteorological Society*, 146(730), 1999-2049, <https://doi.org/10.1002/qj.3803>, 2020.
- 615 Hernandez-Jaramillo, D.C., Medcraft, C., Braga, R.C., Butcherine, P., Doss, A., Kelaher, B., Rosenfeld, D. and
616 Harrison, D.P.: New airborne research facility observes sensitivity of cumulus cloud microphysical
617 properties to aerosol regime over the great barrier reef. *Environmental science: atmospheres*, 4(8), 861-
618 871, 2024.
- 619 Hernandez-Jaramillo, D.C., Harrison, L., Gunner, G., McGrath, A., Junkermann, W., Lief, W., Hacker, J.,
620 Rosenfeld, D., Kelaher, B. and Harrison, D.P.: First generation outdoor marine cloud brightening trial
621 increases aerosol concentration at cloud base height. *Environmental research letters*, 20(5), 054065, 2025.
- 622 Hong, Song-You, Yign Noh, and Jimy Dudhia: A new vertical diffusion package with an explicit treatment of
623 entrainment processes. *Monthly weather review* 134.9, 2318- 2341, <https://doi.org/10.1175/MWR3199.1>,
624 2006.
- 625 Huang, Yi, Siems, Steven T, Manton, Michael J, Rosenfeld, Daniel, Marchand, Roger, McFarquhar, Greg M, and
626 Protat, Alain: What is the Role of Sea Surface Temperature in Modulating Cloud and Precipitation
627 Properties over the Southern Ocean? *Journal of Climate*, 29(20), 7453–7476.
628 <https://doi.org/10.1175/JCLI-D-15-0768.1>, 2016.
- 629 Hughes, T. P., et al. Global warming and recurrent mass bleaching of corals. *Nature*, 543, 373–377, 2017.



- 630 Janjić, Zaviša I.: Comments on “Development and evaluation of a convection scheme for use in climate models”.
631 *Journal of the Atmospheric Sciences* 57.21:3686-3686, [https://doi.org/10.1175/1520-0469\(2000\)057<3686:CODAEO>2.0.CO;2](https://doi.org/10.1175/1520-0469(2000)057<3686:CODAEO>2.0.CO;2), 2000,
632
- 633 Latham, J., Kleypas, J., Hauser, R., Parkes, B., and Gadian, A.: Can marine cloud brightening reduce coral
634 bleaching?. *Atmospheric Science Letters*, 14(4), 214-219, 2013.
- 635 Latham, J., Rasch, P., Chen, C.-C., Kettles, L., Gadian, A., Gettelman, A., Morrison, H., et al. Global temperature
636 stabilization via controlled albedo enhancement of low-level maritime clouds. *Philosophical*
637 *Transactions of the Royal Society A*, 366(1882), 3969–3987, 2008.
- 638 Latham, J.: Control of global warming. *Nature* 347(6291): 339-340. DOI: 10.1038/347339b0, 1990.
- 639 Latham, J.: Amelioration of global warming by controlled enhancement of the albedo and longevity of low-level
640 maritime clouds. *Atmospheric Science Letters*, 3(2-4), 52-58, 2002.
- 641 Mauger, G. S., and Norris, J. R.: Assessing the impact of meteorological history on subtropical cloud fraction.
642 *Journal of climate*, 23(11), 2926-2940, 2010.
- 643 Mlawer, E. J., Taubman, S. J., Brown, P. D., Iacono, M. J., and Clough, S. A.: Radiative transfer for
644 inhomogeneous atmospheres: RRTM, a validated correlated-k model for the longwave. *J. Geophys. Res.*
645 *Atmos.*, 102, 16663, doi: 10.1029/97JD00237, 1997.
- 646 Possner, A., Wang, H., Wood, R., Caldeira, K., and Ackerman, T. P.: The efficacy of aerosol–cloud radiative
647 perturbations from near-surface emissions in deep open-cell stratocumuli. *Atmospheric Chemistry and*
648 *Physics*, 18(23), 17475-17488, 2018.
- 649 Richards, L. S., Siems, S. T., Huang, Y., Zhao, W., Harrison, D. P., Manton, M. J., and Reeder, M. J.: The
650 meteorological drivers of mass coral bleaching on the central Great Barrier Reef during the 2022 La Niña.
651 *Scientific reports*, 14(1), 1-17, 2024.
- 652 Rosenfeld, D., Zhu, Y., Wang, M., Zheng, Y., Goren, T., and Yu, S.: Aerosol-driven droplet concentrations
653 dominate coverage and water of oceanic low-level clouds. *Science*, 363(6427), eaav0566, 2019.
- 654 Saffin, L., Lock, A., Tomassini, L., Blyth, A., Böing, S., Denby, L., and Marsham, J.: Kilometer-scale simulations
655 of trade-wind cumulus capture processes of mesoscale organization. *Journal of Advances in Modeling*
656 *Earth Systems*, 15(3), e2022MS003295, 2023.
- 657 Seifert, A., Heus, T., Pincus, R., and Stevens, B.: Large-eddy simulation of the transient and near-equilibrium
658 behavior of precipitating shallow convection. *Journal of Advances in Modeling Earth Systems*, 7(4),
659 1918-1937, 2015.
- 660 Seifert, A. and Heus, T.: Large-eddy simulation of organized precipitating trade wind cumulus clouds, *Atmos.*
661 *Chem. Phys.*, 13, 5631–5645, <https://doi.org/10.5194/acp-13-5631-2013>, 2013.
- 662 Stevens, B., and Feingold, G.: Untangling aerosol effects on clouds and precipitation in a buffered system. *Nature*,
663 461(7264), 607-613, 2009.
- 664 Thompson, G., and Eidhammer, T.: A study of aerosol impacts on clouds and precipitation development in a large
665 917 winter cyclone. *Journal of the atmospheric sciences*, 71(10), 3636-3658,
666 <https://doi.org/10.1175/JAS-D-918-13-0305.1>, 2014.
- 667 Tollefson J.: Can artificially altered clouds save the Great Barrier Reef? *Nature*. Aug;596(7873):476-478. doi:
668 10.1038/d41586-021-02290-3. PMID: 34433949, 2021.
- 669 Twomey, S.: The influence of pollution on the shortwave albedo of clouds. *Journal of the Atmospheric Sciences*,
670 34(7), 1149–1152, 1977.



- 671 Wang, X., Zhang, L., and Moran, M. D.: Uncertainty assessment of current size-resolved parameterizations for
672 below-cloud particle scavenging by rain. *Atmospheric Chemistry and Physics*, 10(12), 5685-5705, 2010.
- 673 Wang, H., Rasch, P. J., and Feingold, G.: Manipulating marine stratocumulus cloud amount and albedo: a process-
674 modelling study of aerosol-cloud-precipitation interactions in response to injection of cloud condensation
675 nuclei. *Atmospheric Chemistry and Physics*, 11(9), 4237-4249, 2011.
- 676 Weston, M. J., Piketh, S. J., Burnet, F., Broccardo, S., Denjean, C., Bourriane, T., and Formenti, P.: Sensitivity
677 analysis of an aerosol-aware microphysics scheme in Weather Research and Forecasting (WRF) during
678 case studies of fog in Namibia. *Atmospheric Chemistry and Physics*, 22(15), 10221-10245, 2022.
- 679 Wood, R.: Stratocumulus clouds. *Monthly weather review*, 140(8), 2373-2423, 2012.
- 680 Wood, R., and Bretherton, C. S.: On the relationship between stratiform low cloud cover and lower-tropospheric
681 stability. *Journal of climate*, 19(24), 6425-6432, 2006.
- 682 Wood, R., and Ackerman, T. P.: Defining success and limits of field experiments to test geoengineering by marine
683 cloud brightening. *Climatic Change*, 121(3), 459-472, 2013.
- 684 Zhang, Y., Stevens, B., and Ghil, M.: On the diurnal cycle and susceptibility to aerosol concentration in a
685 stratocumulus-topped mixed layer, *Quart. J. Roy. Met. Soc.*, 131, 1567–1583, s2005.
- 686 Zhao, W., Huang, Y., Siems, S., and Manton, M.: The role of clouds in coral bleaching events over the Great
687 Barrier Reef. *Geophysical Research Letters*, 48(14), e2021GL093936, 2021.
- 688 Zhao, W., Huang, Y., Siems, S., Manton, M., and Harrison, D.: Interactions between trade wind clouds and local
689 forcings over the Great Barrier Reef: a case study using convection-permitting simulations. *Atmospheric
690 chemistry and physics*, 24(9), 5713-5736, 2024.